RSC Advances

PAPER

View Article Online
View Journal | View Issue

Cite this: *RSC Adv.*, 2017, **7**, 40383

Super-hierarchical Ni/porous-Ni/V_2O_5 nanocomposites†

Yuan Yue,[a] Lian Ma,[b] Jingze Sun,[c] Hae-Kwon Jeong[ac] and Hong Liang *[ab]

Received 8th June 2017
Accepted 9th August 2017

DOI: 10.1039/c7ra06446b

rsc.li/rsc-advances

Hierarchical nanomaterials are of great interest due to their unique surface properties such as large surface area and high reactivity. In the present research, super-hierarchical (porous-) nickel hosted vanadium oxide (Ni/porous-Ni/V_2O_5) nanocomposite was fabricated using a simple, low-cost, and environmentally-friendly method. A nickel substrate was electrodeposited with vertical pores of ~10 μm in diameter through hydrogen bubbles as "dynamic templates". Two-dimensional V_2O_5 nanosheets were subsequently synthesized directly on the Ni/porous-Ni substrate surface using a hydrothermal method followed by annealing. Peony-like micro-configuration of V_2O_5 was found and crystallography was confirmed using high-resolution characterization. Further analysis indicated that the interface was formed between Ni (111) and V_2O_5 (100). The small lattice mismatch of 1.2% at the interface facilitated the 2D directional growth of V_2O_5 nanosheets on the Ni surface. The specific surface area and porosity of annealed Ni/porous-Ni/V_2O_5 nanocomposite was as high as 15.3 m^2 g^{-1} and 55.1%. The advantage of the structure was found in the heat dissipation. Such super-hierarchical structure is anticipated to be used in applications such as coatings to improve cooling of macro- and micro-devices.

1. Introduction

Hierarchical two-dimensional (2D) nanomaterials have unique morphologies leading to interesting surface, physical, and chemical properties.[1] The unique characteristics such as high specific surface area, large surface porosity, and increased reaction activity have led to various applications, such as catalysis,[2] self-assembly,[3] energy conversion or storage,[4] sensing,[5] drug delivery,[6] among many others.[7–9] To date, various experimental approaches have been utilized to fabricate hierarchical 2D nanostructures. The most common ones are hydrothermal or solvothermal treatment,[10] electrodeposition,[11] spin coating based assembly,[12] physical/chemical vapor deposition,[13] wet-chemical synthesis,[14] electrospinning or spray related methods,[15] template-assisted coating techniques (including Langmuir–Blodgett technique),[16] and self-assembly of nanoparticles.[17] By adjusting experimental conditions, it is possible to fabricate nanomaterials of different components, dimensions, and morphology. Among above mentioned methods, hydrothermal or solvothermal treatment has advantages in terms of uniformity of size and morphology, well-defined crystallinity, and being suitable for mass production. In addition, the electrodeposition can create uniform coatings with crystallized structures. The hydrothermal and electrodeposition are widely adapted methods to fabricate hierarchical 2D nanomaterials.[18–20]

In this research, we propose to combine a metallic substrate with metallic oxides in order to generate novel super-hierarchical composites. The driving force is the firm and conductive support from a metallic substrate to the high reactivity of metallic oxide. The integrated approach has been reported.[21–23] It is a method of facile, low-cost, and environmentally-friendly. There are a large number of recently-published literature referring to the direct growth of metal oxide nanostructure on a metallic substrate. The versatile applications of those metal–metal-oxide composites include the electrochemical energy storage,[24–26] photocalysis,[27,28] gas detection,[29–32] and photovoltaic devices.[33] However, there are two major challenges in controlling the quality and morphology of metal–metal-oxide nanocomposites. One is to select the right materials as metal substrate and metal oxide deposit to ensure the firm physical contact. The other is the rational design in effective experimental routes to fabricate the composite simply, cost-effectively, and environmentally-friendly. Hence, the optimized experimental fabrications overcoming of those two challenges are necessary to be further investigated.

In this research, a novel super-hierarchical Ni/porous-Ni/V_2O_5 nanocomposite was designed and synthesized through a simple two-step approach. The V_2O_5 nanoparticles were selected to be synthesized because of their unique two-dimensional (2D)

[a]Department of Materials Science and Engineering, Texas A&M University, 3003 TAMU, College Station, Texas 77843-3003, USA. E-mail: hliang@tamu.edu
[b]Department of Mechanical Engineering, Texas A&M University, 3123 TAMU, College Station, Texas 77843-3123, USA
[c]Department of Chemical Engineering, Texas A&M University, 3127 TAMU, College Station, Texas 77843-3127, USA

† Electronic supplementary information (ESI) available. See DOI: 10.1039/c7ra06446b

morphology and fruitful properties such as electrochemical activity, abundant reserves, and cost-effective fabrications.[34–37] For the first time, those particles were directly fabricated onto the Ni/porous-Ni substrate. In the first step of fabrication, a microstructured Ni layer was electrodeposited using a previously reported method.[38] Vertically-aligned micro-channels were formed as the unique and characteristic as-electrodeposited Ni/porous-Ni substrate. During the electrodeposition, the streams of hydrogen bubbles formed on the surface of the Ni sheet resulted in the selective deposition of Ni. The formation of Ni micro-channels was the consequence of this selective deposition. Subsequently, the bubbles acted as a "dynamic template", another unique feature for the synthesis. The reason to choose Ni was its ease and reliability to fabricate. In the second step, the nanostructure of vanadium pentoxide (V_2O_5) had grown directly on the Ni/porous-Ni substrate through a facile hydrothermal route. After annealing, lamellar nanostructures of ultrathin 2D V_2O_5 nanosheets arrays and multilayered micro-peonies were formed on the Ni/porous-Ni surface. The emerging of V_2O_5 micro-peonies was the result of the growth and Ostwald ripening during the hydrothermal process. Moreover, the formation mechanism of ultrathin 2D V_2O_5 nanosheet arrays on Ni/porous-Ni was explained according to an atomic structure model. The small lattice mismatch of 1.2% between Ni [212] direction on (111) facet and V_2O_5 [001] promoted the direct growth of 2D V_2O_5 nanosheets on Ni/porous-Ni substrate. The evolution of the super-hierarchical nanostructure could be ascribed as the synergistic effect of the substrate and deposit that were both highly hierarchical. Owing to the ultrahigh surface area of V_2O_5 nanosheets and micro-peonies, the super-hierarchical Ni/porous-Ni/V_2O_5 nanocomposite possessed an excellent heat dissipation. Such structures can be applied to the novel surface coating to prevent the overheating of macro- and micro-devices.[39–43]

2. Experimental methods

2.1. Fabrication of Ni/porous-Ni substrate

The samples of micro-channeled Ni/porous-Ni substrate were fabricated using a facile electrodeposition method. Firstly, the as-purchased 200 Ni sheet (McMaster-Carr, Inc., 99.0% Ni, 0.13 mm thickness) was cleaned by the ultrasonication baths in the deionized (DI) water (Millipore), 0.1 M HNO_3 aqueous solution, and ethanol. After drying the as-cleaned Ni sheet, the electrodeposition was conducted as the galvanostatic mode. A homemade double-electrode set-up including Ni sheet as cathode, graphite rod (6 mm in diameter, 99.995% carbon, Sigma-Aldrich) as anode, and an aqueous electrolyte of 0.2 M $NiCl_2$ (98%, Sigma-Aldrich) and 4.0 M NH_4Cl (≥99.5%, Sigma-Aldrich) was used for the electrodeposition. The applied current density and duration of electrodeposition were fixed as 0.5 A cm^{-2} and 7 minutes, respectively. After electrodeposition of Ni/porous-Ni substrate, it was rinsed by acetone, deionized (DI) water, and ethanol thoroughly. Finally, the vacuum drying of the Ni/porous-Ni substrate was accomplished at 60 °C overnight.

2.2. Synthesis of V_2O_5 2D nanosheets

The multilayered and hierarchical 2D V_2O_5 nanosheets and micro-peonies were grown on the Ni/porous-Ni substrate through a hydrothermal treatment. 0.5 mmol (90.9 mg) of V_2O_5 bulk powder (99.99% trace metals basis, Sigma-Aldrich) was firstly suspended in 23.5 mL DI water by magnetic stirring. After the formation of a uniformly distributed orange blur suspension, 1.5 mL H_2O_2 solution (30% w/w in H_2O, contains stabilizer Sigma-Aldrich) was added into the suspension dropwise. The transparency of the suspension mixture started increasing after continuous stirring for 10 minutes. The suspension completely became a clear and transparent solution with a little bubbling after 30 more minutes stirring at room temperature. This light-orange-colored solution was then transferred to a sealed Teflon hydrothermal autoclave. The as-fabricated micro-channeled Ni/porous-Ni substrate was directly placed into the solution inside the autoclave before sealing it. After the hydrothermal process at 180 °C for 7 hours, the sealed autoclave was cooled down naturally in the air. The product of dark green precipitation and the black Ni/porous-Ni/V_2O_5 samples in the colorless transparent liquid was obtained. After rinsing by ethanol and DI water, both precipitation and Ni/porous-Ni/V_2O_5 samples were dried at 70 °C in a vacuum overnight. Then, the annealing procedure was conducted in the Ar gas flow at 350 °C for 30 minutes. The temperature ramp was set as 5 °C min^{-1}. Finally, the product of dark-brown-colored dried powder of V_2O_5 and Ni/porous-Ni/V_2O_5 sample were fabricated.

2.3. Characterizations

The crystalline structures of Ni/porous-Ni and V_2O_5 powders were characterized by the XRD instrument (Bruker D8 Focus Bragg–Brentano short-arm powder diffractometer) with a Cu Kα X-ray source (λ = 1.540598 Å). The morphological characterization of all samples was conducted at the SEM (FERA-3 Model GMH Focused Ion Beam Microscope, Tescan, Inc.) with an acceleration voltage of 10 kV. The EDS experiments were accomplished by the field emission SEM (JSM-7500F, JEOL, Inc.) with an acceleration voltage of 10 kV. The porous volume and estimated Brunauer–Emmet–Teller (BET) surface area were determined by conducting the nitrogen (N_2) adsorption–desorption experiment using ASAP 2010 (Micromeritics Instrument Corporation) at 77 K. Prior to experiments, the samples were degassed in high vacuum at 100 °C overnight to remove adsorbed gases and other impurities. The *in situ* heat dissipation measurement was conducted on a hot plate in atmosphere. An infrared thermal imager (Ti45, Fluke Corporation) was used to capture the infrared images of samples with calibrated temperature indicator.

3. Results and discussion

3.1. Physical characteristics

The as-fabricated Ni/porous-Ni/V_2O_5 nanocomposites have uniform morphology along with well-crystalline structures. Fig. 1 illustrates the overall physical properties of Ni/porous-Ni/V_2O_5 nanocomposites characterized using the low-magnified

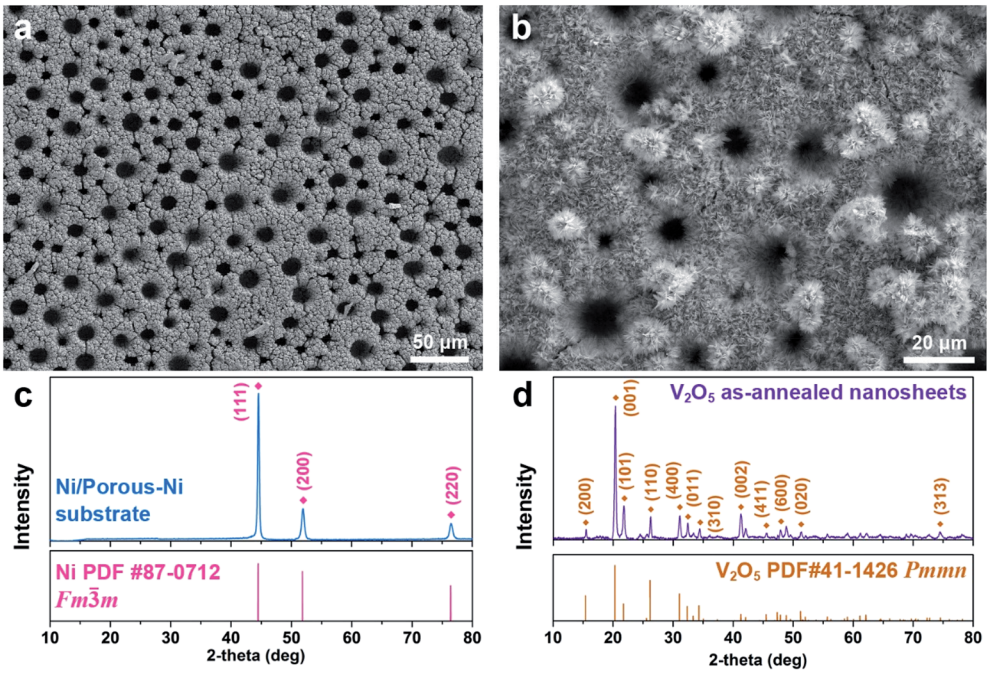

Fig. 1 The low-magnified SEM photographs of (a) Ni/porous-Ni porous substrates (500×) and (b) Ni/porous-Ni/V_2O_5 nanocomposites (1500×). Corresponding XRD patterns of the (c) Ni/porous-Ni substrate and (d) as-annealed V_2O_5 powders.

scanning electron microscopy (SEM) and X-ray diffraction (XRD). The densely distributed vertically-aligned micro-channels of Ni/porous-Ni substrate is exhibited as Fig. 1a. The diameters of those micro-channels span from 10 to 20 μm. According to the previous report,[38] this was the result of selective deposition of Ni owing to the numerous H_2 bubble streams during electrodeposition process. In this case, the streams of bubbles actually played a role of "dynamic templates" to promote the formation of Ni micro-channels. From Fig. 1b, the morphology of V_2O_5 nanostructures can be treated as hierarchical 2D nanosheets. There are two types of the growth of V_2O_5 nanosheets. One is the 2D nanosheets array directly formed on the surface of Ni/porous-Ni substrate. This growth is highly compact and uniform with the full coverage of the surface of Ni/porous-Ni substrate. The other is the multilayered peony-like micro-configuration grown from a large amount of 2D nanosheets. Referring to the crystallographic properties of Ni/porous-Ni/V_2O_5 nanocomposites, two XRD patterns of Ni/porous-Ni substrate and V_2O_5 as-annealed nanosheets are shown in Fig. 1c and d, respectively. The electrodeposited Ni layer with micro-channels has a well-defined face-centered cubic (FCC) structure (JCPDS PDF no. 87-0712, $Fm\bar{3}m$, a = 3.5238 Å). After hydrothermal growth at 200 °C and annealing at 350 °C, the V_2O_5 nanosheets reveal an excellent orthorhombic structure (JCPDS PDF no. 41-1426, $Pmmn$, a = 11.510 Å, b = 3.563 Å, c = 4.369 Å). It is worth noticing in Fig. 1d that a dominating peak of the XRD pattern of V_2O_5 nanosheets is from facet (001). This suggests that the most exposed facet of formed V_2O_5 nanosheets is (001). For the comparison, the crystallinity of as-annealed V_2O_5 nanosheets is much better than that of as-hydrothermal V_2O_5 nanomaterial without annealing (Fig. S1, see ESI†). This indicates the significant role played by the annealing process for the synthesis of well-crystalline V_2O_5 nanosheets.

Our results showed that the Ni/porous-Ni/V_2O_5 nanocomposites have exhibited super-hierarchical nanoarchitecture with evenly composited distribution. Fig. 2 shows this feature. In Fig. 2a, both 2D V_2O_5 nanosheets deposited on Ni surface and the V_2O_5 micro-peonies can be found in a selected region nearby a Ni micro-channel. The uniform and concentrated deposition of 2D V_2O_5 nanosheets array can not only take place on the outer surface of Ni deposit, but the inner wall of micro-channels as well. Meanwhile, multilayered micro-peonies with diameters of 5–10 μm are attached to the nanosheets array. This feature of hierarchical 2D nanostructures directly deposited on the hierarchical micro-sized substrate can be regarded as the "super-hierarchical nanoarchitecture". The morphological details of Ni/porous-Ni/V_2O_5 at the high magnification are revealed in Fig. 2b. The 2D V_2O_5 nanosheets are ultrathin with a thickness lower than 50 nm. The partial translucency of several "nano-petals" of micro-peonies validates this ultrathin feature. The lateral dimensions of single nanosheets are approximately 1–2 μm. Simultaneously, a type of obvious serrated edges can be observed from numerous 2D nanosheets. The slightly different brightness shown in those nanosheets implies a type of stacking of multiple pieces. Usually, this stacking has 3–5 pieces of V_2O_5 nanosheets. Furthermore, the morphological consistency before and after annealing is evaluated through the SEM imaging of an unannealed Ni/porous-Ni/V_2O_5 sample (Fig. S2, see ESI†). Similar morphologies of ultrathin (~50 nm) 2D V_2O_5 nanosheets and micro-peonies can also be observed in the unannealed sample. Whereas, the

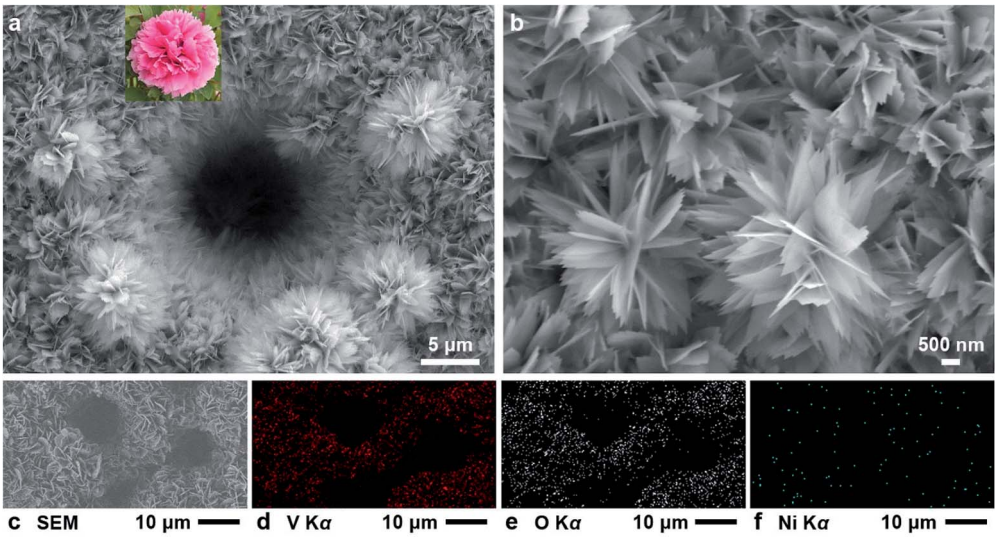

Fig. 2 The medium- and high-magnified SEM photographs and EDS mapping spectrum of Ni/porous-Ni/V_2O_5 nanocomposites. (a) The 5000× SEM image of Ni/porous-Ni/V_2O_5 nanocomposites at the location of one Ni micro-channel. The inset is a photograph of a real blossoming peony. (b) The 15 000× SEM image of several 2D V_2O_5 nanosheets and micro-peonies. (c) The SEM photograph for the region characterized by EDS mapping. The element map of (d) vanadium (Kα), (e) oxygen (Kα), and (f) nickel (Kα).

lateral dimensions of unannealed nanosheets are usually larger (2–4 μm) than those of annealed counterparts. The shrinkage of lateral sizes was the consequence of the crystallization during the annealing procedure. According to the BET nitrogen gas adsorption–desorption experimental results, the BET surface areas of Ni/porous-Ni/V_2O_5 nanocomposites before and after annealing were 10.2 $m^2 g^{-1}$ and 15.3 $m^2 g^{-1}$, respectively. Those values were 40–60 and 6000–8500 times greater than BET surface area of Ni/porous-Ni substrate (2.8×10^{-1} $m^2 g^{-1}$) and surface area of as-cleaned Ni sheet (1.80×10^{-3} $m^2 g^{-1}$, details provided in ESI†). Meanwhile, the volumetric porosity of Ni/porous-Ni substrate and Ni/porous-Ni/V_2O_5 nanocomposites before and after annealing were determined as 47.1%, 54.9%, and 55.1%, respectively. These results revealed the ultrahigh specific surface area and enhanced porosity of super-hierarchical Ni/porous-Ni/V_2O_5 nanocomposites. The hierarchical and multilayered V_2O_5 nanosheets and micro-peonies were the main reason of the increased surface area. Moreover, the uniformity of the spatial distribution of elements is evidenced through the X-ray energy dispersive spectroscopic (EDS) element mapping. After selecting a random area including a large amount of 2D V_2O_5 nanosheets and several Ni micro-channels (as shown in Fig. 2c), the element mapping of vanadium (V, Fig. 2d), oxygen (O, Fig. 2e), and nickel (Ni, Fig. 2f) were obtained. The uniform and abundant distribution of both elements of V (at% ~27%) and O (at% ~64%) from Fig. 2d and e suggested that the numerous 2D nanosheets observed in Fig. 3c were V_2O_5. The rare but even distribution of Ni (at% ~9%) from Fig. 2e confirmed the virtually complete hindering of Ni/porous-Ni substrate by 2D V_2O_5 nanosheets.

3.2. Growth mechanism

The lamellar 2D morphology of V_2O_5 nanosheets on the Ni/porous-Ni substrate was the result of directional growth of V_2O_5 nanocrystals. Fig. 3 is a general schematic illustration of the formation mechanisms of V_2O_5 nanostructures. For this Ni/porous-Ni/V_2O_5 nanocomposite, the formation mechanism of ultrathin 2D V_2O_5 nanosheets and micro-peonies is necessary to be investigated. This is quite significant in order to utilize this novel super-hierarchical nanoarchitecture. Through the crystallographic analysis, a set of models was proposed in this research. According to the fundamentals of the crystallography, V_2O_5 possesses a type of complicated orthorhombic phase.[44] As shown in Fig. 3a, each vanadium atom (white balls) is embedded by a distorted pyramid composed of four oxygen atoms (red balls). Eight corners of a V_2O_5 unit cell are occupied by vanadium atoms.[45] The connection of adjacent VO_5 pyramids forms a 2D single layer in *a*–*b* plane. The weak bonding along *c* direction results in the layered crystalline structure of V_2O_5.[34] When considering the direct growth of the 2D V_2O_5 nanosheets on the surface of Ni/porous-Ni substrate, the most exposed crystalline facets of both V_2O_5 and Ni were analyzed at first. Since the highest XRD peaks of Ni/porous-Ni substrate and V_2O_5 nanosheets were (111) and (001), two regulations could be summarized based on similar analysis in previous researches.[35,36,46] (1) The electrodeposited Ni layer had a most-common surface facet of (111); (2) the double sides of the 2D V_2O_5 nanosheets had the Miller index of (001). This suggested that the ultrathin 2D V_2O_5 nanosheets were composed of *c*-directional stacking of a series of planes combined by VO_5 pyramids.

The formation of ultrathin V_2O_5 nanosheets was the result of the 2D hydrothermal growth from the $[VO_2]^+$ precursor. This precursor was obtained after mixing V_2O_5 powders and H_2O_2 solution before hydrothermal process. According to the related researches, the reactions between bulk V_2O_5 and H_2O_2 with the participation of H_2O at room temperature are listed below:[47–49]

$$V_2O_5 + 4H_2O_2 \rightarrow 2[VO(O_2)_2(OH_2)]^- + 2H^+ + H_2O \quad (1)$$

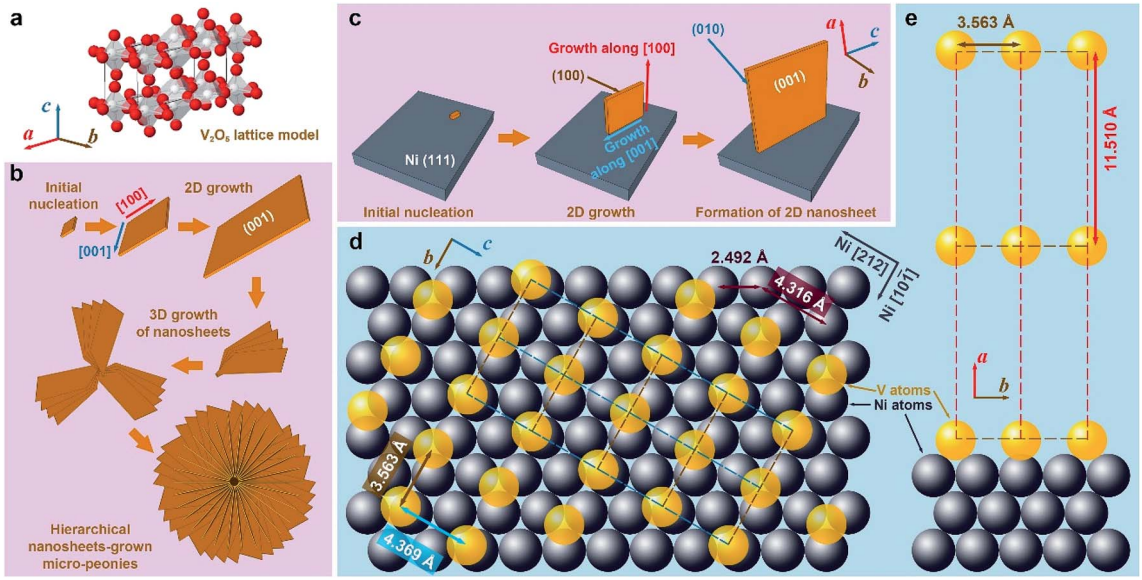

Fig. 3 The schematic illustration of the formation mechanism of Ni/porous-Ni/V_2O_5 nanocomposites. (a) The model of crystalline lattice structure of V_2O_5. The formation procedure of (b) V_2O_5 micro-peonies and (c) 2D V_2O_5 nanosheets on Ni/porous-Ni substrate. The (d) top view and (e) side view of the atomic structure model of V_2O_5 crystal on the Ni (111) substrate. Note: for the simplification, only the vanadium atoms that are located at the corners of the V_2O_5 unit cell of are depicted in (d) and (e).

$$V_2O_5 + 2H^+ + 4H_2O_2 + 3H_2O \rightarrow 2[VO(O_2)(OH_2)_3]^+ + O_2 \quad (2)$$

$$2[VO(O_2)_2(OH_2)]^- + 4H^+ + 2H_2O \rightarrow 2[VO(O_2)(OH_2)_3]^+ + O_2 \quad (3)$$

$$2[VO(O_2)(OH_2)_3]^+ \rightarrow 2[VO_2]^+ + O_2 + 6H_2O \quad (4)$$

The ions of $[VO_2]^+$ along with O_2 gas and water molecules are final products of those reactions. That was the reason why the clear and light-orange-colored solution with some bubbles was obtained after stirring (Fig. S3, see ESI†). During the subsequent hydrothermal treatment, the $[VO_2]^+$ ions acted as the role of vanadium (V^{5+}) source provider. The ultrathin nanosheets of V_2O_5 were gradually formed in the supercritical condition offered by the hydrothermal process.[49] To validate the procedure of 2D hydrothermal growth, the time-dependent SEM imaging of hydrothermal treatment for 1 h, 2 h, 4 h, and 7 h are shown in Fig. 4. The gradual formation of the 2D morphology from preliminary nucleation to lamellar micro-peonies during the first 4 hours can be observed through SEM panels of Fig. 4a–c. From Fig. 4d, 7 hour dense and compact growth of micro-peonies even virtually hinder the Ni micro-channels. Considering the most exposed facet of (001) of 2D V_2O_5 nanosheets, the formation procedure of them could be described as the 2D growth of V_2O_5 crystals along [100] and [001] directions after forming initial nucleation. Fig. 3b and c depict this process. During the 2D growth of ultrathin V_2O_5 nanosheets, the preference of the smaller total surface energy promoted the approaching of neighboring nanosheets to assemble into multilayered micro-peonies (as illustrated in Fig. 3b). The structure of micro-peonies were stable due to the minimization of the total surface energy.[37,50,51] Furthermore, the process of Ostwald ripening was also one reason of the micro-peony formation.[52]

Further study was conducted on the mechanisms of atomic-scale formation of ultrathin 2D V_2O_5 nanosheets directly on the surface of Ni (111) surface. As sketched in Fig. 3c, the V_2O_5 nanosheets are grown through a similar manner of 2D growth along [100] and [001] directions in the hydrothermal condition. It is necessary to point out that the facet of V_2O_5 nanosheets interfacing the Ni (111) plane can be determined as (100). This is based on the analysis of the crystalline structures of Ni (111) plane and V_2O_5 unit cells. An atomic structure model illustrated as Fig. 3d and e was constructed to illustrate the evolution. One necessary condition to form a crystalline material on the surface of another similar to the epitaxial growth is the small lattice mismatch between two crystals.[53–57] According to the crystallographic data obtained through the XRD peak identification in an aforementioned part of this paper, the FCC Ni (111) facet has the interatomic distance of 2.492 Å. Therefore, the distance between two nearest Ni atoms (grey spheres in Fig. 3d and e) along [212] direction is 4.316 Å (as marked in Fig. 3d). On the other side, the orthorhombic V_2O_5 (100) facet has the lattice parameters as 3.563 Å (along *b* direction) and 4.369 Å (along *c* direction), which are also marked in Fig. 3d. Thanks to the small lattice mismatch of 1.2% between 4.369 Å and 4.316 Å, the vanadium atoms (yellow spheres in Fig. 3d and e) on the facet (100) can be packed on the Ni (111) surface along [212] and [10$\bar{1}$] directions. Axes of V_2O_5 *b* and *c* are corresponding to the directions of Ni [10$\bar{1}$] and $\overline{212}$, respectively. The form of packing of vanadium atoms at the corner of the orthorhombic V_2O_5 lattice is demonstrated as Fig. 3d and e. Through this packing the most exposed facet of the V_2O_5 nanosheets is (001). This is consistent with the experimental measurement using XRD. As noted that the oxide of V_2O_5 directly grew on the metallic Ni surface and the ions of

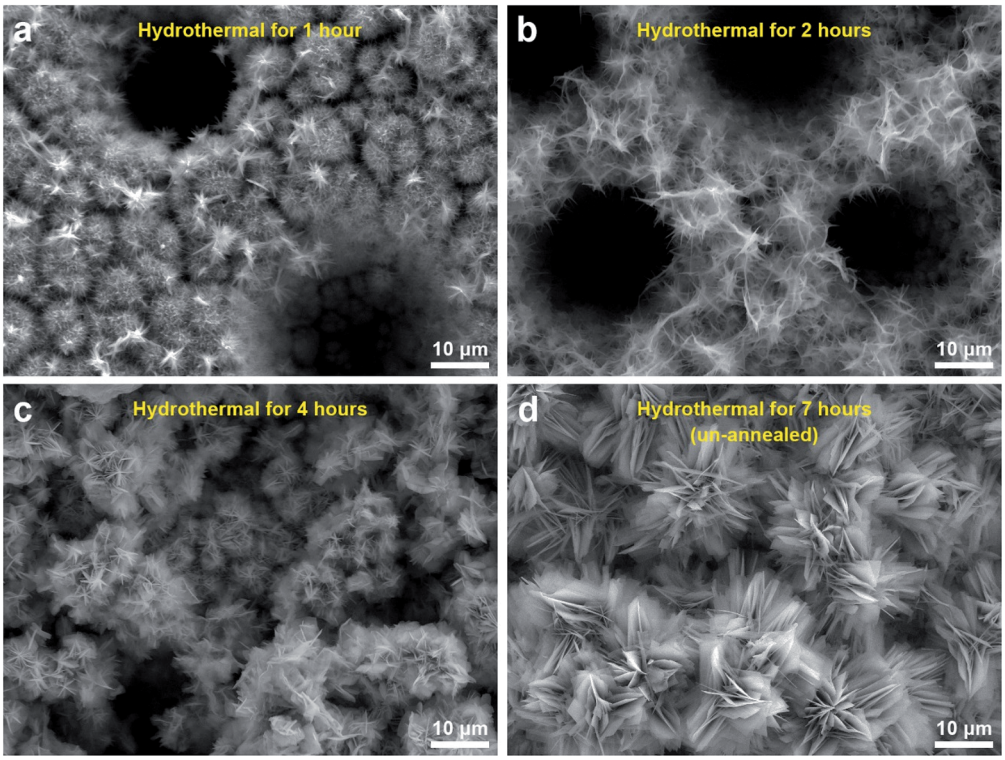

Fig. 4 The time-dependent SEM images of hydrothermal treatment at 200 °C for (a) 1 h, (b) 2 h, (c) 4 h, and (d) 7 h (before annealing).

O^{2-} acted as the natural binder. It is anticipated that there is no clear interface formed.

3.3. Heat dissipation

Heat dissipation of the super-hierarchical Ni/porous-Ni/V_2O_5 nanocomposite was characterized using an *in situ* heating and cooling process. For comparison, seven samples were tests. They are as-cleaned Ni, Ni/porous-Ni substrate, Ni/porous-Ni/V_2O_5 after 1 h, 2 h, 4 h, and 7 h (annealed and unannealed) hydrothermal treatments at 200 °C. After placing 7 samples at the center of a hot plate as illustrated in Fig. 5a. A slow and uniform heating was started at room temperature of 27 °C (300 K). The surface temperature of the hot plate reached 49.3 °C after 25 min of heating. The power was then turned off and the plate was cooled in air. For another 25 min, surface temperature of the hot plate reached 32 °C. Fig. 5b–m illustrate the *in situ* time-dependent infrared thermal images of the samples. It was clear to observe that the surface temperature T of Ni/porous-Ni/V_2O_5 after 7 h hydrothermal treatment with annealing was the highest, meaning the highest thermal conductivity. Meanwhile, the surface temperature of as-cleaned Ni was the lowest, the least conductive. This was evidenced in both heating and cooling cycle. The detailed data points of the surface temperatures of 7 samples and hot plate are depicted in Fig. 5n. The trend of $T_{7\ \text{h-an}} > T_{7\ \text{h-un}} > T_{4\ \text{h}} > T_{2\ \text{h}} > T_{1\ \text{h}} > T_{\text{Ni/porous-Ni}} > T_{\text{Ni}}$ was discovered that can be seen at any time point during the heating–cooling cycle. The higher the surface temperature, the greater the dissipated heat flow,[41,43] the values of Q followed the rule of $Q_{7\ \text{h-an}} > Q_{7\ \text{h-un}} > Q_{4\ \text{h}} > Q_{2\ \text{h}} > Q_{1\ \text{h}} > Q_{\text{Ni/porous-Ni}} > Q_{\text{Ni}}$.

In this research, the regulation of Fourier's law for the heat conduction was applied to investigate the heat dissipation performance. Eqn (5) describes the formula of Fourier's law.[58]

$$Q = qA = -kA\frac{\mathrm{d}T}{\mathrm{d}x} \tag{5}$$

Parameters of q, A, and k are heat flux density, surface area, and thermal conductivity of the sample. $\mathrm{d}T/\mathrm{d}x$ is the gradient of the temperature from one side of sample to the other. In the present work, $\mathrm{d}T/\mathrm{d}x$ can be rewritten as $(T_{\text{plate}} - T_{\text{room}})/d$ as the temperature gradient is linear, where d is the thickness of all samples, *i.e.* ~0.13 mm. Hence, at a specific time point during heating and cooling, values of $(T_{\text{plate}} - T_{\text{room}})/d$ as well as $\mathrm{d}T/\mathrm{d}x$ of all 7 samples were nearly identical. According to reported data, the thermal conductivity of V_2O_5 thin nanosheets ranged 0.45–1.7 W m^{-1} K^{-1}.[59,60] Although the thermal conductivity of 200 Ni was 70 W m^{-1} K^{-1},[58] the value of product of $(kA)_{7\ \text{h-an}}$ was still approximately 150 times higher than $(kA)_{\text{Ni}}$. The main reason was the ultrahigh specific surface area of the super-hierarchical Ni/porous-Ni/V_2O_5 nanocomposite. The ultrahigh surface area was far enough to compensate the intrinsic low thermal conductivity of V_2O_5 thin nanosheets. As a result, $Q_{7\ \text{h-an}}$ was the greatest among all 7 samples at any moment during the heating and cooling. As a result, the super-hierarchical Ni/porous-Ni/V_2O_5 nanocomposite exhibited superior heat dissipation efficiency. This unprecedented characteristic indicates the potential to be used as novel surface coatings to improve cooling effect for macro- and micro-devices.

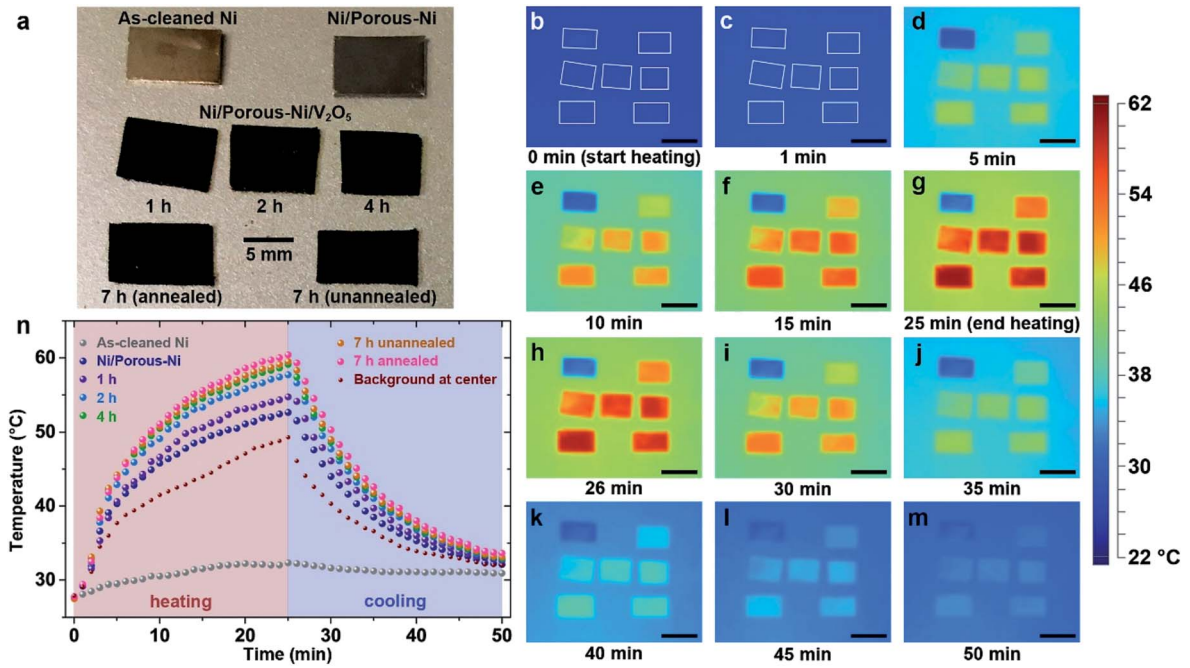

Fig. 5 The enhanced heat dissipation performance of the Ni/porous-Ni/V_2O_5 nanocomposites. (a) The digital camera photograph of the samples of as-cleaned Ni, Ni/porous-Ni substrate, Ni/porous-Ni/V_2O_5 nanocomposites after hydrothermal treatment for 1 h, 2 h, 4 h, 7 h (both before and after annealing). (b)–(m) The time-dependent infrared thermal images of samples during an *in situ* heating and cooling procedure. The heating and cooling durations are 25 min. The scale bars are 1 cm. The white rectangles in (b) and (c) mark the locations of 7 samples. (n) The plot of the temperature change of all samples and the central point of background during the heating and cooling procedure.

4. Conclusion

To summarize, a super-hierarchical Ni/porous-Ni/V_2O_5 nanocomposite was fabricated using a simple, low-cost, and environmentally-friendly two-step approach of electrodeposition followed by hydrothermal treatment. A nickel substrate was electrodeposited with vertically-aligned micro-channels of ~10 μm in diameter through hydrogen bubbles as "dynamic templates". Two distinguished nanostructures were generated, 2D V_2O_5 nanosheets (<50 nm thick) and peony-like microconfiguration. These two structures were evolved directly on the Ni/porous-Ni substrate surface using a hydrothermal and annealing process. Through the BET nitrogen adsorption–desorption experiment, the specific surface area and porosity of the annealed Ni/porous-Ni/V_2O_5 nanocomposite was determined as 15.3 $m^2\ g^{-1}$ and 55.1%. The growth mechanism of such hierarchical morphology of V_2O_5 nanostructures was investigated. Firstly, XRD analysis indicated that 2D crystal grew along the directions of [100] and [001] from the $[VO_2]^+$ precursor. Furthermore, micro-peonies were the result of the growth and Ostwald ripening inside the supercritical fluid. An atomic crystalline model was generated to illustrate the interfacial relationship, the low lattice mismatch (1.2%) between directions of FCC Ni [212] and orthorhombic V_2O_5 [001] promoted the packing of vanadium atoms of facet (100) on the Ni (111) surface. Furthermore, the superior heat dissipation performance of super-hierarchical Ni/porous-Ni/V_2O_5 sample was discovered through *in situ* thermal imaging. This unique characteristic was attributed to the ultrahigh surface area. The great thermal energy released through the Ni/porous-Ni/V_2O_5 sample was beneficial to applications in effective cooling when the material is made as coatings. Overall, the easy fabrication, unique super-hierarchical structures, and ultrahigh surface area open new avenues for future investigation. The advanced structure generated in this research will facilitate the usage of Ni/porous-Ni/V_2O_5 composites for the application of surface coating to prevent the overheating of macro- and micro-devices.

Conflicts of interest

Authors have no conflicts of interests.

Acknowledgements

The authors would like to thank Dr W. Kuo from the Materials Characterization Facility of Texas A&M University for his assistance with the SEM imaging. This research is partially sponsored by the Turbomachinery Laboratory at the Texas A&M University, the Texas A&M University's Strategic Initiative seed grant program, and Oscar S. Wyatt Jr Professorship endowment. The open access publishing fees for this article have been covered by the Texas A&M University Open Access to Knowledge Fund (OAKFund), supported by the University Libraries and the Office of the Vice President for Research.

References

1 R. Lakes, *Nature*, 1993, **361**, 511–515.
2 J. Pérez-Ramírez, C. H. Christensen, K. Egeblad, C. H. Christensen and J. C. Groen, *Chem. Soc. Rev.*, 2008, **37**, 2530–2542.
3 R. Schreiber, J. Do, E.-M. Roller, T. Zhang, V. J. Schüller, P. C. Nickels, J. Feldmann and T. Liedl, *Nat. Nanotechnol.*, 2014, **9**, 74–78.
4 Y. Yue and H. Liang, *J. Power Sources*, 2015, **284**, 435–445.
5 Y. Liu, Y. Jiao, Z. Zhang, F. Qu, A. Umar and X. Wu, *ACS Appl. Mater. Interfaces*, 2014, **6**, 2174–2184.
6 M. Vallet-Regí, F. Balas and D. Arcos, *Angew. Chem., Int. Ed.*, 2007, **46**, 7548–7558.
7 A. Gupta, T. Sakthivel and S. Seal, *Prog. Mater. Sci.*, 2015, **73**, 44–126.
8 Y. Yue, Y. Kan, H. Choi, A. Clearfield and H. Liang, *Appl. Phys. Lett.*, 2015, **107**, 253103.
9 W. Dai, B. Kheireddin, H. Gao and H. Liang, *Tribol. Int.*, 2016, **102**, 88–98.
10 K. Byrappa and T. Adschiri, *Prog. Cryst. Growth Charact. Mater.*, 2007, **53**, 117–166.
11 J. Qiu, M. Guo, Y. Feng and X. Wang, *Electrochim. Acta*, 2011, **56**, 5776–5782.
12 D. Xia, A. Biswas, D. Li and S. R. Brueck, *Adv. Mater.*, 2004, **16**, 1427–1432.
13 H. Liu, L. Feng, J. Zhai, L. Jiang and D. Zhu, *Langmuir*, 2004, **20**, 5659–5661.
14 U. Nithiyanantham, A. Ramadoss and S. Kundu, *RSC Adv.*, 2014, **4**, 35659–35672.
15 W.-E. Teo and S. Ramakrishna, *Compos. Sci. Technol.*, 2009, **69**, 1804–1817.
16 L. J. Cote, F. Kim and J. Huang, *J. Am. Chem. Soc.*, 2008, **131**, 1043–1049.
17 H. Qiu, Z. M. Hudson, M. A. Winnik and I. Manners, *Science*, 2015, **347**, 1329–1332.
18 K. Shehzad, Y. Xu, C. Gao and X. Duan, *Chem. Soc. Rev.*, 2016, **45**, 5541–5588.
19 Y. Tang, X. Rui, Y. Zhang, T. M. Lim, Z. Dong, H. H. Hng, X. Chen, Q. Yan and Z. Chen, *J. Mater. Chem. A*, 2013, **1**, 82.
20 L. Yang, M. Zhang, K. Zhu, J. Lv, G. He and Z. Sun, *Appl. Surf. Sci.*, 2017, **391**, 353–359.
21 X. Du, Q. Wang, T. Feng, X. Chen, L. Li, L. Li, X. Meng, L. Xiong, X. Sun and L. Lu, *Sci. Rep.*, 2016, **6**, 20138.
22 Y. Yue, F. Wu, H. Choi, C. Shaver, M. Sanguino, J. Staffel and H. Liang, *Surf. Coat. Technol.*, 2017, **309**, 523–530.
23 K. Takahashi, Y. Wang and G. Cao, *J. Phys. Chem. B*, 2005, **109**, 48–51.
24 K. Cao, L. Jiao, H. Liu, Y. Liu, Y. Wang, Z. Guo and H. Yuan, *Adv. Energy Mater.*, 2015, **5**, 1401421.
25 X. Du, Q. Wang, T. Feng, X. Chen, L. Li, L. Li, X. Meng, L. Xiong, X. Sun and L. Lu, *Sci. Rep.*, 2016, **6**, 20138.
26 J. Yuan, C. Chen, Y. Hao, X. Zhang, R. Agrawal, W. Zhao, C. Wang, H. Yu, X. Zhu and Y. Yu, *J. Alloys Compd.*, 2017, **696**, 1174–1179.
27 Q. Lu, Y. Yu, Q. Ma, B. Chen and H. Zhang, *Adv. Mater.*, 2016, **28**, 1917–1933.
28 R. Saravanan, S. Joicy, V. K. Gupta, V. Narayanan and A. Stephen, *Mater. Sci. Eng., C*, 2013, **33**, 4725–4731.
29 R. Vander Wal, G. Hunter, J. Xu, M. Kulis, G. Berger and T. Ticich, *Sens. Actuators, B*, 2009, **138**, 113–119.
30 J. Zhang, X. Liu, G. Neri and N. Pinna, *Adv. Mater.*, 2016, **28**, 795–831.
31 E. Comini, *Mater. Today*, 2016, **19**, 559–567.
32 K. Schneider, M. Lubecka and A. Czapla, *Sens. Actuators, B*, 2016, **236**, 970–977.
33 S. K. Balasingam, M. G. Kang and Y. Jun, *Chem. Commun.*, 2013, **49**, 11457–11475.
34 N. A. Chernova, M. Roppolo, A. C. Dillon and M. S. Whittingham, *J. Mater. Chem.*, 2009, **19**, 2526–2552.
35 K. Dewangan, N. N. Sinha, P. G. Chavan, P. K. Sharma, A. C. Pandey, M. A. More, D. S. Joag, N. Munichandraiah and N. S. Gajbhiye, *Nanoscale*, 2012, **4**, 645–651.
36 X. Rui, Z. Lu, H. Yu, D. Yang, H. H. Hng, T. M. Lim and Q. Yan, *Nanoscale*, 2013, **5**, 556–560.
37 A. Q. Pan, H. B. Wu, L. Zhang and X. W. D. Lou, *Energy Environ. Sci.*, 2013, **6**, 1476–1479.
38 C. Marozzi and A. Chialvo, *Electrochim. Acta*, 2000, **45**, 2111–2120.
39 A. Tomitaka, K. Ueda, T. Yamada and Y. Takemura, *J. Magn. Magn. Mater.*, 2012, **324**, 3437–3442.
40 K. H. Kim, Y. Oh and M. F. Islam, *Adv. Funct. Mater.*, 2013, **23**, 377–383.
41 H. Rho, S. Lee, S. Bae, T.-W. Kim, D. S. Lee, H. J. Lee, J. Y. Hwang, T. Jeong, S. Kim and J.-S. Ha, *Sci. Rep.*, 2015, **5**, 12710.
42 S. M. Jung, D. J. Preston, H. Y. Jung, Z. Deng, E. N. Wang and J. Kong, *Adv. Mater.*, 2016, **28**, 1413–1419.
43 P. Liu, Z. Fan, A. Mikhalchan, T. Q. Tran, D. Jewell, H. M. Duong and A. M. Marconnet, *ACS Appl. Mater. Interfaces*, 2016, **8**, 17461–17471.
44 Y. Wang and G. Cao, *Chem. Mater.*, 2006, **18**, 2787–2804.
45 Y. Yue and H. Liang, *Adv. Energy Mater.*, 2017, **7**, 1602545.
46 B. Qu, L. Hu, Q. Li, Y. Wang, L. Chen and T. Wang, *ACS Appl. Mater. Interfaces*, 2013, **6**, 731–736.
47 C. J. Fontenot, J. W. Wiench, M. Pruski and G. Schrader, *J. Phys. Chem. B*, 2000, **104**, 11622–11631.
48 Y. Liu, M. Clark, Q. Zhang, D. Yu, D. Liu, J. Liu and G. Cao, *Adv. Energy Mater.*, 2011, **1**, 194–202.
49 J. Zhu, L. Cao, Y. Wu, Y. Gong, Z. Liu, H. E. Hoster, Y. Zhang, S. Zhang, S. Yang, Q. Yan, P. M. Ajayan and R. Vajtai, *Nano Lett.*, 2013, **13**, 5408–5413.
50 A. Böker, J. He, T. Emrick and T. P. Russell, *Soft Matter*, 2007, **3**, 1231–1248.
51 M. M. Rahman, A. Z. Sadek, I. Sultana, M. Srikanth, X. J. Dai, M. R. Field, D. G. McCulloch, S. B. Ponraj and Y. Chen, *Nano Res.*, 2015, **8**, 3591–3603.
52 L. Zhou, Z. Zhuang, H. Zhao, M. Lin, D. Zhao and L. Mai, *Adv. Mater.*, 2017, **29**, 1602914.
53 W. I. Park, D. H. Kim, S.-W. Jung and G.-C. Yi, *Appl. Phys. Lett.*, 2002, **80**, 4232–4234.
54 B. Lalmi, H. Oughaddou, H. Enriquez, A. Kara, S. Vizzini, B. Ealet and B. Aufray, *Appl. Phys. Lett.*, 2010, **97**, 223109.
55 M. Zhou, W. Ming, Z. Liu, Z. Wang, P. Li and F. Liu, *Proc. Natl. Acad. Sci. U. S. A.*, 2014, **111**, 14378–14381.

56 S. Kim, A. A. Polycarpou and H. Liang, *Appl. Surf. Sci.*, 2015, **351**, 460–465.
57 C. Tan and H. Zhang, *J. Am. Chem. Soc.*, 2015, **137**, 12162–12174.
58 W. D. Callister and D. G. Rethwisch, *Materials science and engineering: an introduction*, Wiley, New York, 2007.
59 M. Kang, S. W. Kim, J.-W. Ryu, Y. Xu and R. Kato, *J. Korean Phys. Soc.*, 2013, **62**, 1134–1138.
60 R. Santos, J. Loureiro, A. Nogueira, E. Elangovan, J. Pinto, J. Veiga, T. Busani, E. Fortunato, R. Martins and I. Ferreira, *Appl. Surf. Sci.*, 2013, **282**, 590–594.